# Additively Manufactured Ti-5Al-5V-5Mo-3Cr: Understanding Defect-Fatigue Relationships

Mohammad Salman Yasin<sup>1,2</sup>, Alireza Jam<sup>1,2</sup>, Mahdi Habibnejad-Korayem<sup>3</sup>, Meysam Haghshenas<sup>4</sup>, Shuai Shao<sup>1,2</sup>, Nima Shamsaei<sup>1,2,\*</sup>

<sup>1</sup>National Center for Additive Manufacturing Excellence (NCAME), Auburn University, Auburn, AL 36849, USA

<sup>2</sup>Department of Mechanical Engineering, Auburn University, Auburn, AL 36849, USA <sup>3</sup>External R&D, AP&C- a GE Additive Company, St-Eustache, QC, J7R 0L5, Canada <sup>4</sup>Fatigue, Fracture and Failure Laboratory (F3L), Department of Mechanical, Industrial and Manufacturing Engineering, The University of Toledo, Toledo, OH 43606, USA

> \* Corresponding author: shamsaei@auburn.edu Tel: (334) 844-4839

Submitted to: International Journal of Fatigue

Original Submission: March 2024 Revised Submission: May 2024

#### Abstract

Ti-5Al-5Mo-5V-3Cr (Ti-5553), a near-β Ti alloy, possesses an excellent combination of strength, toughness, and strength-to-weight ratio, and due to its poor machinability characteristic, it is poised to be additively manufactured for key structural applications. This study examines the micro-/defect-structure and mechanical behavior, including both tensile and fatigue, of laser powder bed fused Ti-5553. The tensile and fatigue specimens are fabricated in two locations on the build plate with respect to the powder feed direction, i.e., west (away from powder reservoir) and east (near powder reservoir), to examine the location dependence of the mechanical properties. In addition, fatigue specimens are furnished in both un-machined and machined surface conditions. It is found that the volumetric defect content is higher for the west specimens than the ones in the east; however, tensile and fatigue properties are not affected by part location. The insensitivity of fatigue lives to the part location can be ascribed to specimens having statistically equivalent defect size distribution near the surface, as fatigue failures are primarily initiated by critical defects on or in the vicinity of the surface in un-machined and machined specimens.

**Keywords:** Laser powder bed fusion (L-PBF); Titanium alloy; Tensile properties; Fatigue; Part location

# Nomenclature

Critical defect size measured based on Murakami's method from fractography						
Square root of the projected area of a defect in the plane perpendicular to the loading direction measured from XCT data						
Defect size corresponding to 50th percentile probability of occurrence						
Dimension of a defect along the specimen's radial direction						
Fatigue strength exponent						
Confidence interval						
Elongation to failure						
Specimens near powder reservoir						
Probability density function						
Cumulative density function						
Distance of defect from the specimen surface						
Arithmetic mean surface roughness						
Maximum profile valley depth						
Goodness of fit						
Ultimate tensile strength						
Specimens away from the powder reservoir						
Yield strength						
Reversals to failure						
Extreme values distribution shape parameter						
Extreme values distribution location parameter						
Relative density						
Stress amplitude						
Fatigue strength coefficient						

# **Abbreviations**

AM	Additive manufacturing/ additively manufactured
BSE	Backscattered electron
EBSD	Electron backscattered diffraction
LL	Likelihood length
L-PBF	Laser powder bed fusion/ laser powder bed fused
NHT	Non-heat treated
SEM	Scanning electron microscope/microscopy
Ti-5553	Ti-5Al-5Mo-5V-3Cr
Ti-64	Ti-6Al-4V
XCT	X-ray computed tomography

#### 1. Introduction

The near-β Ti alloy Ti-5Al-5Mo-5V-3Cr (Ti-5553), developed in the 1990s, possesses excellent combination of strength, toughness, and strength-to-weight ratio and has thus become a promising candidate for the key structural applications in airframes, including load-bearing fuselage components, and landing gears [1–3]. These components often have complex shapes and, given Ti-5553's poor machinability, are found often challenging to fabricate via conventional processing routes. In this regard, additive manufacturing (AM), with its net shaping capability, can be a reasonable alternative for these Ti-5553 parts considering their low-production nature. Among the different AM processes, laser powder bed fusion (L-PBF) is particularly appealing because of its outstanding dimensional accuracy and compatibility with Ti-5553 due to the alloy's decent welding characteristics [4,5].

The layer-by-layer fabrication strategy, high cooling rates, repeated remelting and solidification, and high dynamic melt pools that characterize L-PBF processes can induce surface texture [6–8], microstructural anomalies [9–11], and volumetric defects [12–14] that are sensitive to even slight perturbations in process/design parameters [15]. The resulting materials' unique micro-/defect-structure together with their variability can lead to mechanical properties—especially fatigue—that not only drastically differ from those of the wrought counterparts but also contain significant uncertainty [16]. For Ti-6Al-4V (Ti-64), a popular Ti alloy among the AM community and aerospace industry with many overlapping applications with Ti-5553, L-PBF often induces fine martensitic microstructure and populous volumetric defects. The defect content within Ti-64 parts appears to depend on both the reuse state of the feedstock and part location [17]. Specifically, it has been shown that while light reuse can improve the powder's flowability and reduce defect population in parts, continued reuse causes excessive oxygen pickup which promotes

defect formation due to spattering, especially in the regions near the shield gas exhaust. Even after extensive post-processing, including annealing and surface machining, the fatigue behavior of laser powder bed fused (L-PBF) Ti-64 is still generally governed by volumetric defects, which is partially due to its fine lamellar  $\alpha + \beta$  microstructure. Although the microstructure can be further coarsened by prolonged soaking at elevated temperatures [18], this coarsening is highly heterogenous and forms large globular  $\alpha$  grains, which is detrimental to mechanical properties [19–21].

In contrast, L-PBF Ti-5553 responds well to heat treatments and can be furnished in a relatively wide combination of strength and ductility. Although its microstructure comprises almost completely  $\beta$  columnar grains in the as-solidified state [22–24], which is quite ductile, Ti-5553 can be heat treated to be  $\alpha + \beta$  by age hardening [25,26]. Depending on the heat treatment, the strength of the L-PBF Ti-5553 can vary between ~800 MPa and ~1600 MPa and the corresponding elongation between 17.2% and 4.3% [25,26]. The relatively wide variation in microstructure and thus tensile properties can potentially make the fatigue behavior of L-PBF Ti-5553 significantly different from that of other additively manufactured (AM) Ti alloys, e.g., Ti-10V-2Fe-3Al, Ti-6Al-6V-2Sn and Ti-6Al-2Sn-4Zr-6Mo [27]. However, while some limited fatigue data of wrought Ti-5553 and its close variants exists in the open literature [11,28,29], fatigue characteristics of AM Ti-5553, including its sensitivity to volumetric defects and surface texture are still not well understood.

This study investigates the tensile and fatigue behaviors of L-PBF Ti-5553 in two surface conditions: un-machined and machined. Scanning electron microscopy (SEM) and X-ray computed tomography (XCT) are performed to characterize the microstructure and defect contents of Ti-5553. The potential correlation between the micro-/defect-structure and mechanical

behaviors is carefully examined. The effect of part location on the volumetric defect content, surface texture, and the resulting mechanical properties is also analyzed. In addition, the powder characteristics, tensile, and fatigue behaviors of the L-PBF Ti-5553 reported in this work, are compared to both L-PBF Ti-64 and wrought Ti-5553 (wherever applicable) from the literature. Such a comparison is made because of the relatively limited data for AM Ti-5553 and the abundance of AM Ti-64 data in the literature. To the authors' knowledge, this is the first time that the fatigue behavior of AM Ti-5553 has been systematically characterized. Specifically, the correlation between the size of the critical volumetric defects and the fatigue life is constructed. In addition, extreme value statistics has been used to compare the defect sizes obtained from fractography and the XCT to examine any potential effects from part location.

### 2. Experimental procedure

Plasma-atomized Ti-5553 powder supplied by AP&C, a GE Additive company, was used in this study for part fabrication. The chemical composition (in wt.%) of the pre-alloyed Ti-5553 powder, as measured by the manufacturer, is listed in **Table 1**. The powder's particle size distribution was measured using a Coulter LS particle size analyzer following ASTM B822 [30]. The powder had a nominal size distribution of 15-45 μm, with the 10<sup>th</sup>, 50<sup>th</sup>, and 90<sup>th</sup> size percentiles (D<sub>10</sub>, D<sub>50</sub>, and D<sub>90</sub>) of 21 μm, 33 μm, and 44 μm, respectively. Before fabrication, the powder was sieved using an 80 μm mesh to ensure the removal of extremely large particles and agglomerates. To evaluate the flowability, powder samples were taken from the powder reservoir and characterized using aeration and shear tests. These tests were conducted via an FT4 Powder Rheometer® following ASTM D7891 [31] and manufacturer (i.e., Freeman Technology, UK) recommendations [32].

Table 1: Chemical composition of AP&C plasma atomized Ti-5553, as reported by the manufacturer.

Elements	Wt.%
О	0.14
N	< 0.005
C	0.014
Н	0.002
Fe	0.34
Al	5.58
V	4.89
Mo	4.87
Cr	2.89
Others	< 0.20
Ti	Balance

The fabrication of parts was carried out using an EOS M290 machine, a commercial L-PBF system, under an Ar environment. The process parameter set used during the fabrication is listed in **Table 2**. The original equipment manufacturer's recommended process parameters for Ti-64 were directly adopted for Ti-5553 in this study. To verify these parameters, some cylindrical test parts of 5 mm diameter and 15 mm height were printed before this study. XCT performed on these parts revealed an excellent relative density of 99.997 %. Therefore, further optimization of the process parameters was not performed. The build layout, as shown in **Figure 1** (a), consisted of cylindrical rods, fatigue specimens in un-machined surface condition and half-built rods. A few powder capsules and XCT coupons were also included to monitor the print quality, but were not included in this work. To investigate the effect of part location on mechanical behavior, including both tensile and fatigue, the build plate was divided into 2 groups of west and east. The parts near

the powder reservoir were labeled with the prefix "east", and those further away were labeled with the prefix "west". All parts were fabricated vertically with respect to the build platform and were detached from the build plate, annealed at 900 °C (i.e., above the  $\beta$  transus temperature of ~845 °C [33]) in an Ar environment for 1 hour, then furnace-cooled to room temperature.

Table 2: L-PBF process parameters used for the part fabrication.

Laser Power (W)	Laser Speed (mm/s)	Hatch Distance (mm)	Layer Thickness (µm)	Energy Density (J/mm <sup>3</sup> )
280	1200	0.14	30	55.6

Among the 62 cylindrical rods fabricated (100 mm in height and 13 mm in diameter), 24 were used in this study. The rods were machined down to the tensile (4 rods) and fatigue (20 rods) geometries following ASTM E8M [34] and ASTM E466 [35], respectively (Figure 1 (b) and (d)). Moreover, 36 un-machined fatigue specimens with geometry designed according to ASTM E466 [35], as shown in **Figure 1** (c), were fabricated to study the effect of surface condition on the fatigue behavior of Ti-5553. Among which, 23 specimens were used in this study. The half-built rods (referred to hereafter as microstructural samples) were incorporated to examine the microstructure representative of the build height at the gage of the test specimens. The microstructural samples, including non-heat treated (NHT) and annealed ones, were cut from the half-built rods along the longitudinal plane (i.e., the plane parallel to the build direction) and mounted in epoxy resin. The samples were ground using sandpapers with an average grit size ranging from 50 to 2.5 μm, followed by a final polish step with 0.02 μm colloidal silica. Microstructural analyses were carried out using a Zeiss Crossbeam 550 Scanning Electron Microscope (SEM). Electron backscattered diffraction (EBSD) patterns were acquired on samples with a step size of 2.1 µm and an acquisition rate of 40 Hz.

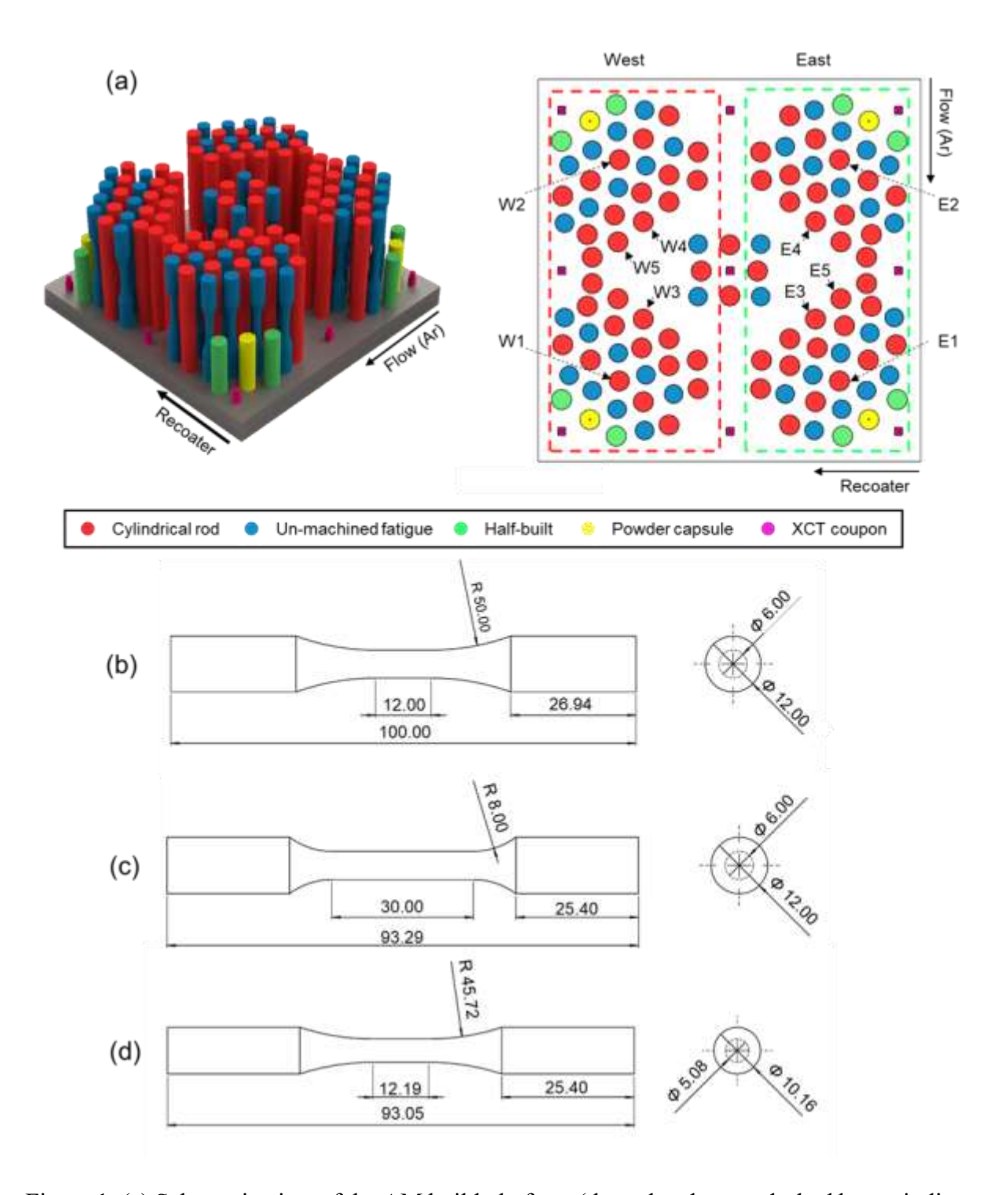


Figure 1: (a) Schematic view of the AM build platform (the red and green dashed boxes indicate west and east groups of the build plate, respectively). (b-d) The geometries and dimensions of the test specimens: (b) un-machined fatigue specimen geometry according to ASTM E466; (c) machined tensile specimen geometry according to ASTM E8M; and (d) machined fatigue specimen geometry according to ASTM E466. Dimensions are in mm.

XCT was performed with an approximate scanned volume of 115 mm<sup>3</sup> to analyze the defect morphology and size distribution on the gage section of fatigue specimens. Two machined fatigue specimens were scanned from each location. The locations of the scanned specimens, i.e., W1, W2 in west and E1 and E2 in east, are shown in **Figure 1** (a). These scans were performed using a ZEISS Xradia 620 Versa machine with a voxel size of 6.5 μm. The source voltage and power used for the analysis were 140 kV and 21 W, respectively. The Xradia Versa proprietary software was used for volumetric reconstruction from the acquired projections. The post-processing of the three-dimensional XCT dataset was carried out using Fiji ImageJ and Dragonfly. To avoid false-positive defect detection from noise, defects with equivalent sphere diameters smaller than 20 μm (i.e., ~3 voxel sizes) were not included in the analysis.

The surface roughness parameters of arithmetic mean height  $(R_a)$  and maximum profile valley depth  $(R_v)$  of all 23 un-machined fatigue specimens were measured. The measurement on each specimen was conducted using a Keyence VHX 6000 digital optical microscope from 5 profile lines of 5 mm length along the build direction in the gage sections.

Six cylindrical rods (W3, W4, W5, E3, E4, and E5 as shown in **Figure 1** (a)) were machined down to the tensile specimen geometry. Quasi-static tensile tests were conducted at 0.001 mm/mm/s nominal strain rate following ASTM E8M [34]. The tensile tests were performed at room temperature using an MTS landmark servo-hydraulic testing machine with 100 kN load cells. The extensometer was removed at 0.05 mm/mm strain to avoid damage due to overtravel. Fully reversed (i.e., stress ratio = -1) force-controlled uniaxial fatigue tests were performed on both un-machined and machined specimens using a 25 kN servo-hydraulic MTS machine according to ASTM E466 [35]. Test frequencies varied from 1.5 to 5 Hz depending on the stress amplitude to ensure nominally the same average cyclic strain rate. The stopping criterion for the

fatigue tests was set as  $\geq 0.5$  mm absolute crosshead displacement. Furthermore, the fatigue tests continued until specimen rupture or run-out for any tests exceeding  $5 \times 10^6$  cycles. The fatigue data were analyzed following the guidelines in ASTM E739 [36]. The fractography of tensile and fatigue specimens was performed using the SEM, and the critical defect sizes ( $\sqrt{\text{area}_{\text{defect},M}}$ ) were calculated based on the Murakami method [37]. This method estimates the effective defect area ( $\text{area}_{\text{defect},M}$ ) of a critical defect by considering a convex contour that envelopes the two-dimensional projection of the defect on the loading plane.

#### 3. Experimental results

#### 3.1 Powder characteristics

The morphology of Ti-5553 powder, characterized with SEM, is shown in **Figure 2**. The Ti-5553 particles were spherical, without significant agglomeration or exceedingly large particles. However, fine satellite particles were also observed. These satellite particles can compromise powder flowability due to increased inter-particle friction and cohesion between the particles [38,39]. **Table 3** lists the rheological properties of the Ti-5553 powder (aeration energy and cohesion) and compares it with the Ti-64 powder used in Ref. [17] which is also plasma atomized and with the particle size distribution of  $D_{10} = 23 \mu m$ ,  $D_{50} = 45 \mu m$ , and  $D_{90} = 57 \mu m$  (this is slightly larger than that of the Ti-5553 powder,  $D_{10} = 21 \mu m$ ,  $D_{50} = 33 \mu m$ , and  $D_{90} = 44 \mu m$ ). With Ti-5553 being a relatively new alloy, the comparison of the rheological properties, i.e., aeration energy and cohesion, between Ti-5553 and Ti-64 powders were made to gain insights into Ti-5553's behavior relative to the well-studied Ti-64. The aeration energy indicates the resistivity of the powder to fluidize by gas flow—lower aeration energy implies better flowability. The cohesion refers to the shear stress needed to slide a layer of powder when there is no applied normal

stress—lower cohesion indicates better flowability. Both aeration energy and cohesion of Ti-5553 were found to be higher than Ti-64, therefore lower powder flowability was expected for Ti-5553 as compared to Ti-64, indicating a higher chance of location dependency being observed in defect-structure and properties of Ti-5553 specimens.

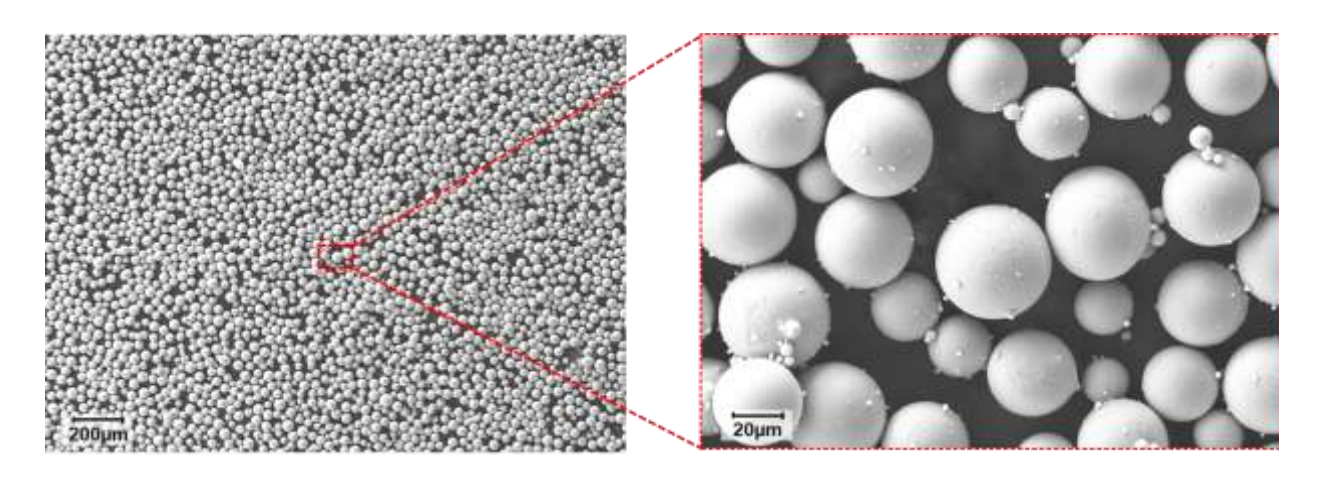


Figure 2: Micrographs of Ti-5553 powder particles obtained using the SEM.

Table 3: Rheological properties of Ti-5553 compared with Ti-64 powder data presented in Ref. [17].

Powder Characteristic	Ti-5553	Ti-64
Aeration energy (mJ)	$7.41 \pm 0.08$	$5.00 \pm 0.30$
Cohesion (kPa)	$0.15\pm0.01$	$0.10\pm0.02$

## 3.2 Micro-/defect-structure and surface roughness analysis

The microstructural features in NHT and annealed L-PBF Ti-5553 are shown in **Figure 3**. While the NHT microstructure exhibited columnar  $\beta$  grains oriented along the build direction

(Figure 3 (a)), the annealed microstructure appeared to be equiaxed (Figure 3 (e)). In addition, there was no apparent crystallographic texture visible from the pole figures of either the NHT or annealed microstructures (see Figure 3 (d) and (h)). The EBSD scans revealed  $\beta$  phase fractions of 99.7% for the NHT microstructure and 92.1% for the annealed one (Figure 3 (b) and (f)). Moreover, after annealing, the  $\alpha$  phase appeared mostly along the  $\beta$  grain boundaries. Higher magnification backscattered electron (BSE) micrographs of both microstructures are shown in Figure 3 (b) and (f). The BSE micrographs revealed the existence of submicron sized  $\alpha$  in the NHT microstructure (higher magnification shown in Figure 3 (c)), in contrast to the needle-like  $\alpha$  near the grain boundary for the annealed microstructure (higher magnification shown in Figure 3 (g)). Note that although the microstructural samples presented in these figures were taken from the west location, similar features were also observed for the east samples.

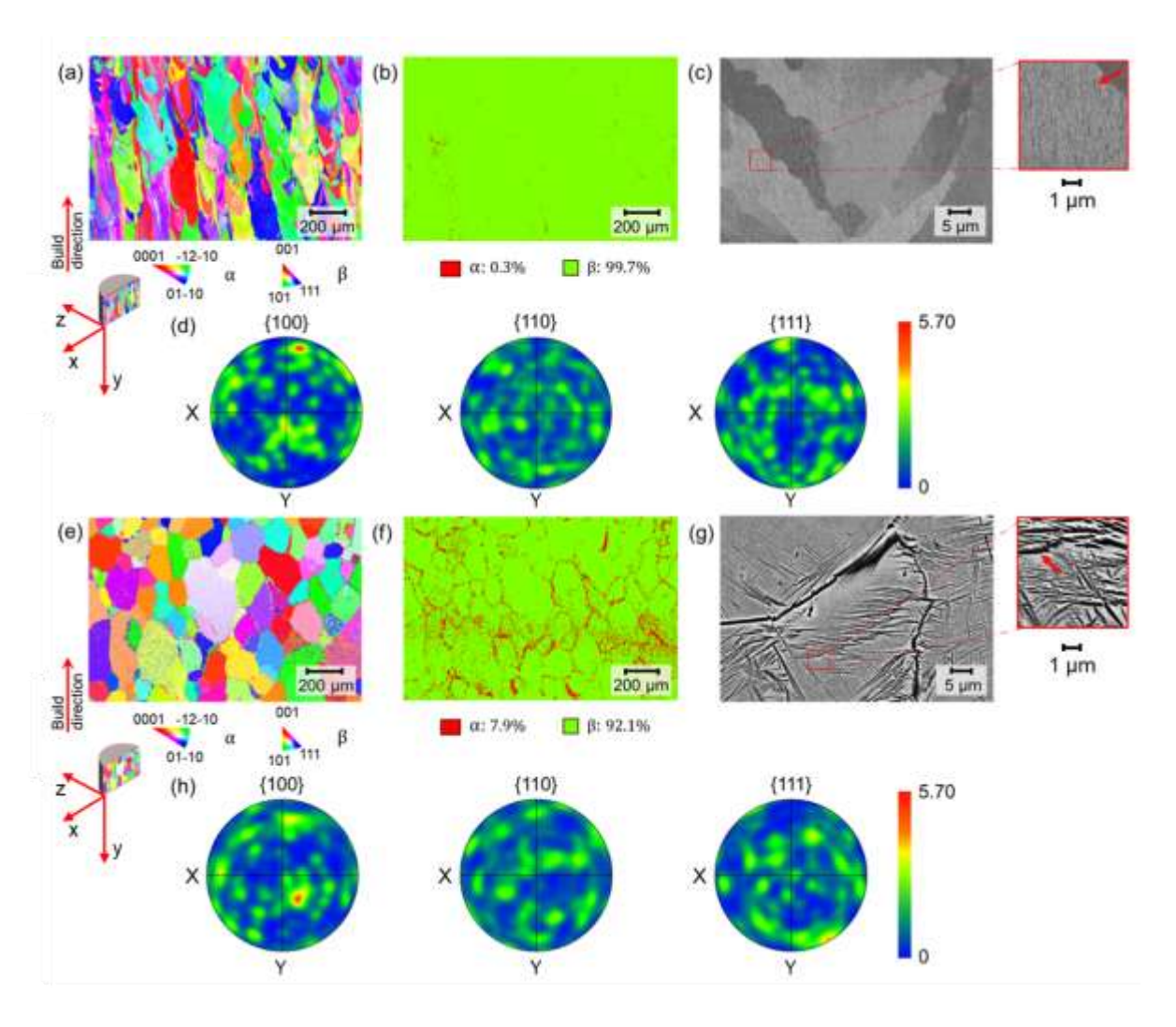


Figure 3: IPF (along the build direction) maps, phase maps, BSE micrographs and pole figures of (a-d) NHT and (e-h) annealed L-PBF Ti-5553. The corresponding phase fractions of  $\alpha$  and  $\beta$  are also labeled on (b) and (e). Red arrows indicate the  $\alpha$  phase in the microstructure.

The 3D visualizations of defect contents in the selected specimens from west (W1 and W2) and east (E1 and E2), obtained from the XCT scans, and their corresponding size distributions are presented in **Figure 4**. The defects were color coded according to their square root of the projected area ( $\sqrt{\text{area}_z}$ ) in the plane perpendicular to the loading direction. The parameter  $\sqrt{\text{area}_z}$  was used as an equivalent defect size estimator similar to Murakami's  $\sqrt{\text{area}_{\text{defect},M}}$  for crack initiating defects [40–42]. The west specimens showed slightly lower relative density ( $\rho_{\text{relative}}$ ), with slightly more defects, compared to the east specimens (**Figure 4** (a) and (b)), which could be attributed to the

poor powder flowability leading to location dependency [38,43]. Moreover, in all specimens, the defects seemed to be randomly distributed, and the majority of the defects were found to be lack of fusions. The largest defect in each scanned volume is also shown for each specimen in **Figure 4** (a) and (b). The defect size distribution calculated based on the √area₂ for west and east specimens is presented in **Figure 4** (c) using box plot and normal distribution curves. The horizontal bars represent the maximum relative frequency of the defect size for each specimen. The relative frequency is calculated as the ratio of counts per bin to the total defect count. Evidently, the west specimens not only had more defects, they also had larger defects compared to the east ones.

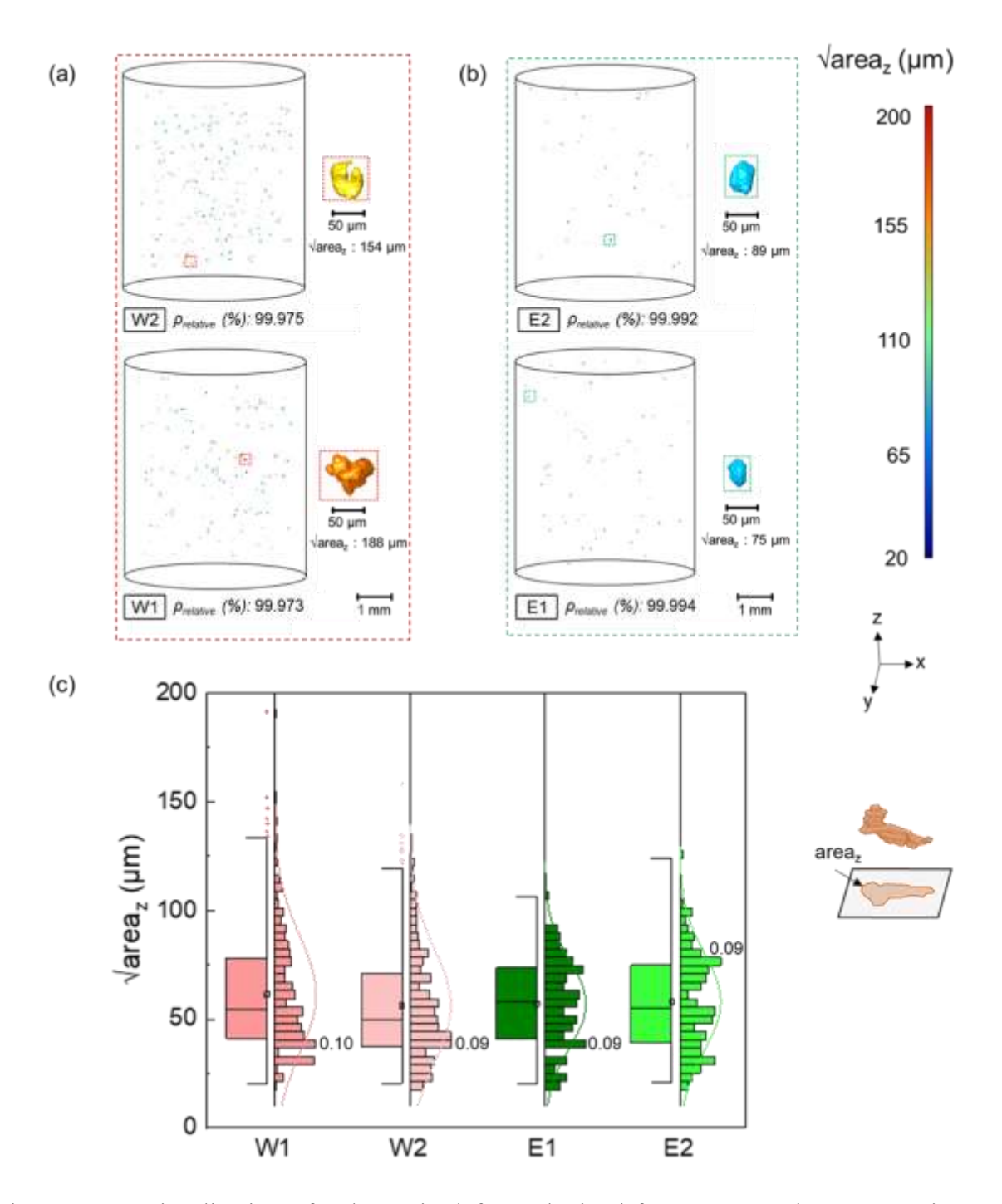


Figure 4: 3D visualization of volumetric defects obtained from XCT at the gage sections of selected specimens from (a) west (W1 and W2) and (b) east (E1 and E2). The largest defect for each specimen is also isolated and visualized. The defects are color coded according to their square root of the projected area ( $\sqrt{area_z}$ ) in the plane perpendicular to the loading direction. (c) Box plot indicating the defect size distributions in those selected specimens. The horizontal bars indicate the relative frequency of the defect size for each specimen, which is calculated as the count per bin over the total defect count.

The surface roughness parameters ( $R_a$  and  $R_v$ ) for un-machined Ti-5553 specimens are shown in **Figure 5** with their respective 90% confidence intervals (CI). These parameters are also compared with those of un-machined Ti-64 presented in Ref. [17]. As mentioned at the end of the introduction, such a comparison with the Ti-64 data as a baseline is meaningful since Ti-5553 is relatively new alloy for L-PBF processes. This was especially the case since manufacturer recommended process parameters of Ti-64 were used for fabricating Ti-5553 and the recommended values for the latter were not available. The west specimens (with  $R_a = 20.7 \pm 3.2$   $\mu$ m and  $R_v = 59.9 \pm 11.6$   $\mu$ m) had slightly lower surface roughness compared to the east specimens (with  $R_a = 23.3 \pm 2.5$   $\mu$ m and  $R_v = 68.0 \pm 10.1$   $\mu$ m). Despite the differences in powder characteristics and alloy chemistry, similar surface roughness values were observed for Ti-5553 and Ti-64. Evidently, the alloy composition had a minimal influence on the surface texture.

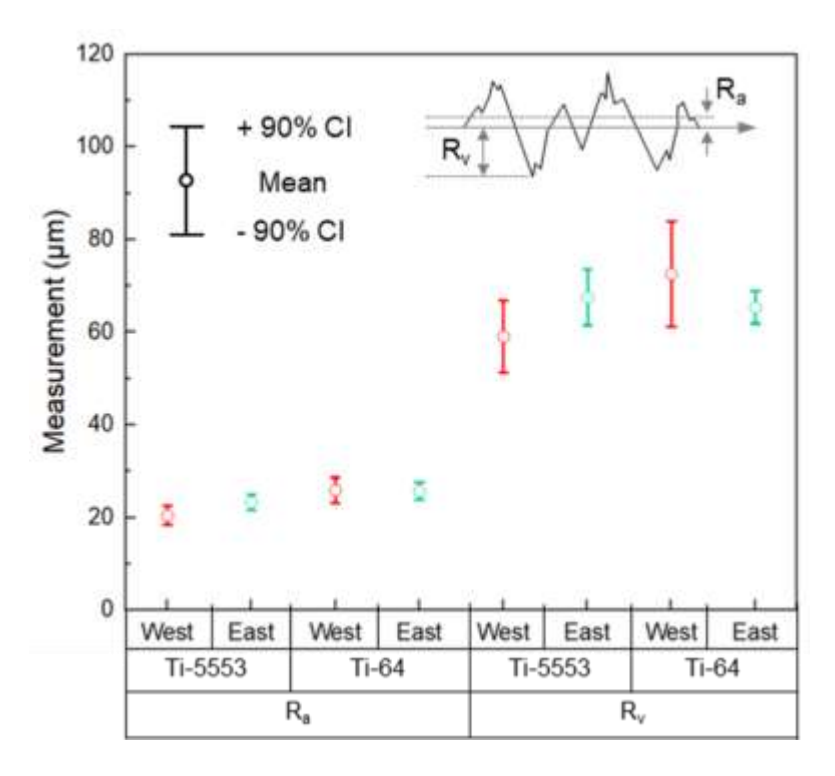


Figure 5: The surface roughness parameters for un-machined L-PBF Ti-5553 specimens and comparison with un-machined L-PBF Ti-64 data presented in Ref. [17].

## 3.3 Tensile properties

The engineering stress-strain curves and quasi-static tensile properties of machined L-PBF Ti-5553 for west and east specimens are presented in **Figure 6** (a) and (b). The tensile properties were also compared with wrought Ti-5553 [44], wrought Ti-64 [45], and machined L-PBF Ti-64 [17]. Note that the comparison was made between the near- $\beta$  alloy (Ti-5553) and the  $\alpha$  +  $\beta$  alloy (Ti-64). For wrought Ti-5553, heat treatment was performed in two conditions: 950 °C for 1 hour (HT1), and 950 °C for 1 hour followed by 700 °C for 4 hours and 500 °C for 6 hours (HT2). The wrought and L-PBF Ti-64 were heat treated at 700 °C for 1 hour and 900 °C for 1 hour, respectively. Overall, the variation between tensile properties of west and east specimens of machined L-PBF Ti-5553 was negligible. Similar insensitivity of tensile properties to part location

was also observed for the L-PBF Ti-64 [17]. This was mostly likely due to the specimens regardless of the location having similar microstructure.

Furthermore, the L-PBF Ti-5553 exhibited a good combination of strength (both yield strength (YS) and ultimate tensile strength (UTS)) and ductility (as measured by elongation to failure (EL)) compared to the others (**Figure 6** (b)), which might be due to their differences in microstructure and chemical composition. The compared HT1 wrought Ti-5553, with substantially lower strengths (e.g., YS of ~760 MPa), had a fully  $\beta$  microstructure with an average grain size of 200-250  $\mu$ m; and the HT2 wrought Ti-5553, with comparable strengths to the L-PBF counterpart studied in this work, consisted of an  $\alpha$ + $\beta$  microstructure [44]. Noting that the average grain size of 231± 56  $\mu$ m was reported for the L-PBF counterpart in this work, the different strengths between the HT1 wrought and L-PBF materials were perhaps due to the different phase compositions. On the other hand, the difference in the tensile properties of the L-PBF Ti-5553 and L-PBF and wrought Ti-64 can be attributed not only to their differing microstructures but also to their variations in chemical compositions.

The fracture surface of a machined L-PBF Ti-5553 specimen after the tensile test is shown in **Figure 7**. The surface could be divided into 2 zones, namely, a fibrous zone in the central region and a shear zone near the outer perimeter. In the fibrous zone, round dimples, indicative of ductile fracture behavior, were evident. Furthermore, cleavage facets, a characteristic feature of brittle fracture, could also be observed in the central region (**Figure 7**). The coexistence of dimples and facets indicated moderately ductile behavior in L-PBF Ti-5553. This tendency towards slight brittleness may be attributed to the presence of grain boundary α [46–48].

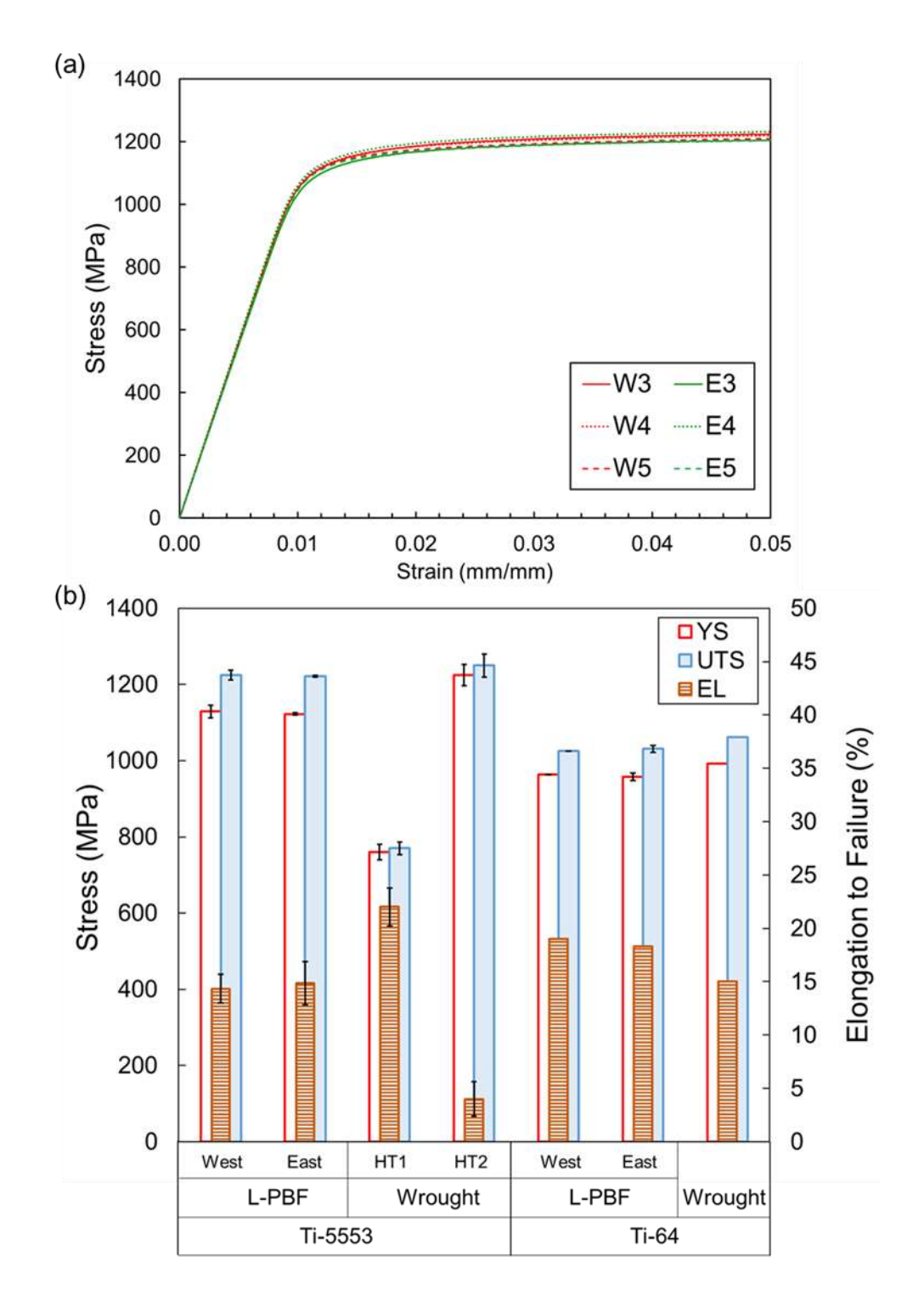


Figure 6: (a) Engineering stress-strain curves of machined L-PBF Ti-5553 specimens from west (W3, W4 and W5) and east (E3, E4 and E5) as well as (b) quasi-static tensile properties of L-PBF Ti-5553 obtained from this study compared with wrought Ti-5553 [40], wrought Ti-64 [41], and machined L-PBF Ti-64 [17].

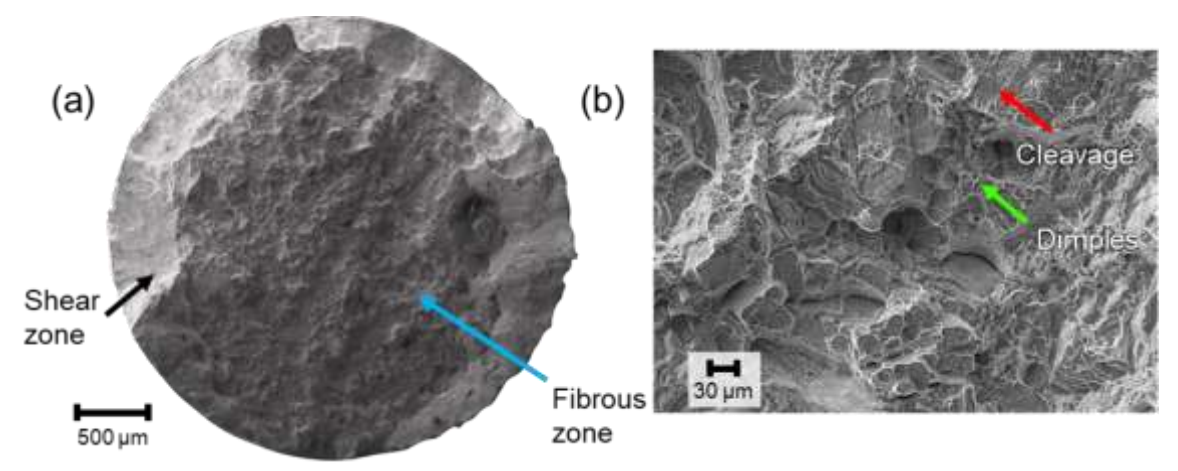


Figure 7: The tensile fracture surface of a machined L-PBF Ti-5553 specimen. Note that black, blue, green, and red arrows point at shear zone, fibrous zone, dimples, and cleavage, respectively.

#### 3.4 Fatigue behavior

Fatigue results of un-machined L-PBF Ti-5553 specimens with details including specimen ID, stress amplitude ( $\sigma_a$ ), reversals to failure ( $2N_f$ ), and part location are listed in **Table 4**. Note that for the un-machined specimens, the crack initiation was always from multiple locations on the specimens' surface. The fatigue results of machined L-PBF Ti-5553 specimens are listed in **Table 5** with more details including location and the critical defect sizes on the fracture surface.

Table 4: Uniaxial, fully-reversed fatigue test results for un-machined L-PBF Ti-5553 specimens.

Specimen ID	$\sigma_a({ m MPa})$	$2N_f$	Defect Location	Specimen Location
SP-09	150	121,868		
SP-20	150	> 10,000,000		
SP-118	150	> 10,000,000		
SP-108	150	89,832		
SP-10	200	192,926	All surface	***
SP-112	200	225,348	225,348 initiation from 57,710 multiple locations	West
SP-18	300	57,710		
SP-111	300	42,634		
SP-19	400	21,374		
SP-110	400	18,932		

SP-17	500	16,022	
SP-109	500	9,998	
SP-45	150	> 10,000,000	
SP-81	150	> 10,000,000	
SP-82	150	> 10,000,000	
SP-34	200	150,042	
SP-89	200	452,420	
SP-44	300	63,960	
SP-80	300	54,856	
SP-43	400	26,396	
SP-79	400	21,626	
SP-35	500	11,760	
SP-90	500	8,108	

Table 5: Uniaxial, fully-reversed fatigue test results for machined L-PBF Ti-5553 specimens.

Specimen ID	$\sigma_a$ (MPa)	$2N_f$	Defect Location	√area <sub>defect,M</sub> (μm)	Specimen Location
SP-15	350	> 10,000,000			
SP-117	350	> 10,000,000			
SP-13	400	191,372	Surface	58	
SP-23	400	> 7,339,506	Grip failure		
SP-115	400	517,596	Surface	61	
SP-12	500	333,838	Internal	51	West
SP-105	500	114,558	Surface	23	West
SP-114	500	52,338	Surface	89	
SP-14	600	143,356	Internal	56	
SP-116	600	109,336	Surface	62	
SP-11	700	22,654	Surface	63	
SP-113	700	28,680	Surface	54	
SP-38	350	> 10,000,000			
SP-88	350	4,921,142	Internal	120	
SP-40	400	9,434,088	Surface	48	
SP-50	400	2,014,460	Surface	154	
SP-86	400	215,732	Surface	61	
SP-41	500	800,836	Internal	51	East
SP-76	500	118,488	Surface	19	
SP-87	500	54,242	Surface	77	
SP-39	600	57,534	Surface	33	
SP-85	600	51,474	Surface	88	
SP-42	700	26,660	Surface	53	

SP-89 700 19,882 Surface 57

The stress-life fatigue data are visualized in **Figure 8** (a) for un-machined and machined surface conditions. The results were also compared to the Ti-64 data presented in Ref. [17], for both un-machined and machined surface conditions in **Figure 8** (b) and (c), respectively. Note that the text in the figures of the format "XE or XW" (where X is an integer) indicated the presence of more than one specimen from east or west group having similar fatigue lives at the respective stress level. The run-out specimens were marked using horizontal arrows. One specimen tested at 400 MPa failed from the grip at 3,669,753 cycles, at which point no gage failure was observed. This specimen is marked using a vertical arrow in **Figure 8** (a) and (c). Significantly shorter fatigue lives were observed for the un-machined specimens compared to the machined ones. The fatigue data for both un-machined and machined conditions regardless of part location were separately fitted using the Basquin relation following ASTM E739 [36], i.e.,

$$\sigma_a = \sigma_f' (2N_f)^b \tag{1}$$

where  $\sigma_a$  is applied stress,  $\sigma'_f$  is fatigue strength coefficient, and b is fatigue strength exponent. The fitted line is shown in **Figure 8** (a) and the corresponding coefficients are shown in **Table 6**. Note that all the specimens in the run-out stress level were not used for the fitting.

Regardless of the part location, the machined specimens showed higher fatigue resistance than un-machined specimens. In addition, the fatigue lives also did not show any significant dependency on the part location. Un-machined specimens exhibited less scatter in fatigue data compared to machined specimens. It could be also noted from **Figure 8** (b) and (c) that the L-PBF

Ti-64, as presented in Ref. [17], showed similar fatigue lives as L-PBF Ti-5553, in both unmachined and machined surface conditions.

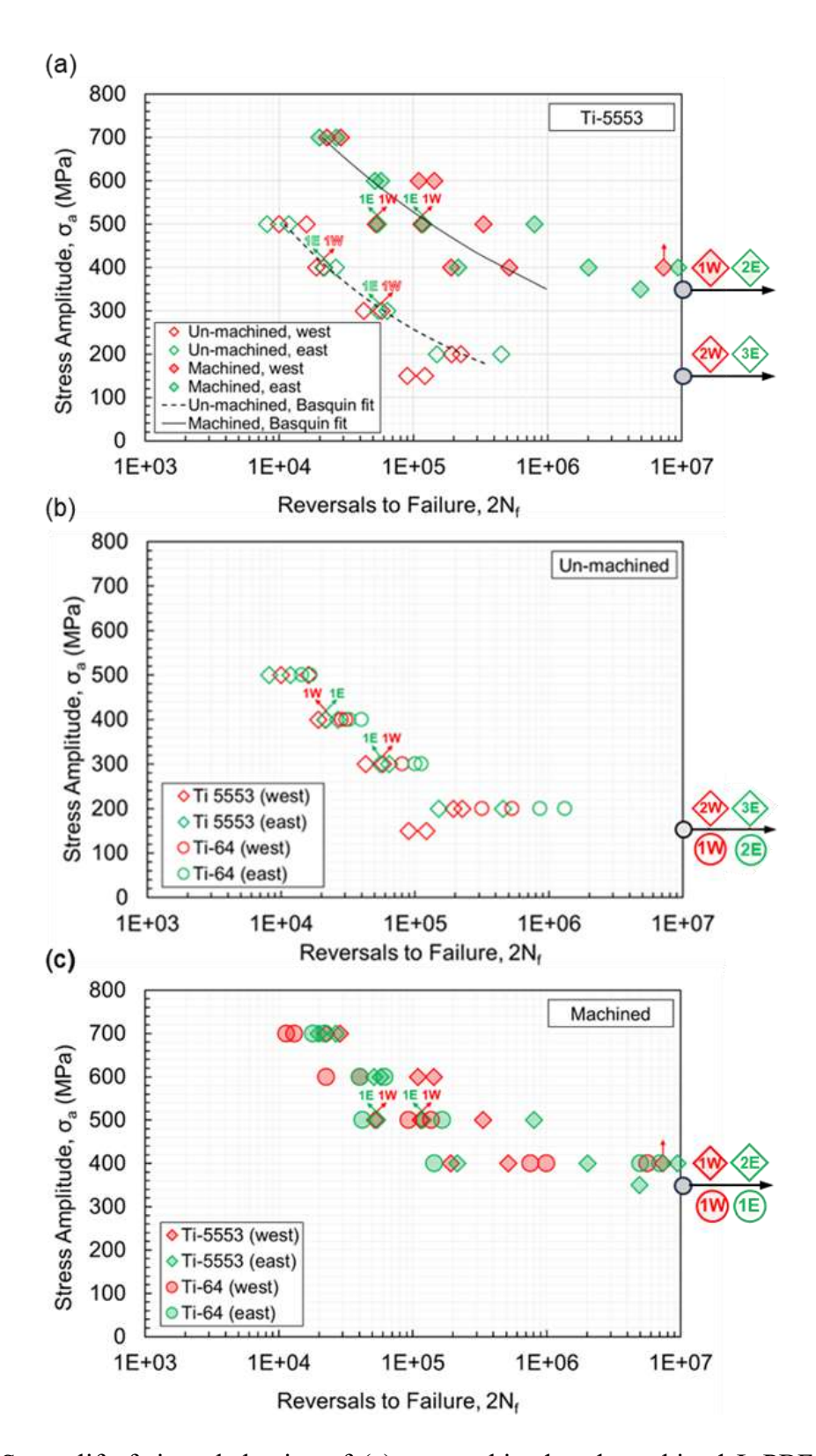


Figure 8: Stress-life fatigue behavior of (a) un-machined and machined L-PBF Ti-5553. A comparison is made with Ti-64 data presented in Ref. [17] for both (b) un-machined and (c) machined conditions.

Table 6: Stress-life fatigue properties for un-machined and machined L-PBF Ti-5553.

Condition	$\sigma_f$	b
Un-machined	8143.7	-0.30
Machined	4189.2	-0.18

#### 4. Discussion

## 4.1 Fatigue behavior and the role of un-machined surface

The fatigue behavior of AM materials, especially in the high cycle fatigue regime, can be sensitive to the presence of both surface and volumetric anomalies. In the un-machined surface condition, the detrimental effect of volumetric anomalies is often overwhelmed by the surface ones. This is evident from the results presented in **Figure 8** (a). In general, the fatigue lives of unmachined specimens, except for the two outlying data points near 10<sup>5</sup> reversals at 150 MPa, did not show a noticeable dependence on the part location (see **Figure 8** (b)), which could be ascribed to the mostly similar surface roughness measures of west and east specimens (**Figure 5**). Indeed, as shown by the fractographic images presented in **Figure 9** (a) and (b), the fatigue crack initiation was consistently from the micro notches in the un-machined surfaces at multiple locations. Some of these micro notches have been indicated using yellow arrows in **Figure 9**. The cracks from the micro notches coalesced into larger cracks and led to the final fracture. Similar crack initiation and growth behavior had already been reported for L-PBF Ti-64 [49–52].

The two outlying west specimens at 150 MPa (shown as red diamonds in **Figure 8** (b)) exhibited significantly shorter fatigue lives, which indicated a potentially different fatigue damage mechanism. To investigate this, the fracture surfaces of the outliers were examined, and the involvement of volumetric defects could be seen in the crack initiation sites (**Figure 9** (c) and (d)).

Specifically, one relatively large, sub-surface volumetric defect (√area<sub>defect,M</sub> of ~90 and 57 μm for SP-09 and SP-108, respectively) was observed in the crack initiation region of each fracture surface. The volumetric defects, given their proximity to the specimen surfaces, may have interacted with the surface notches, which resulted in accelerated initiation of fatigue cracks and shorter fatigue lives.

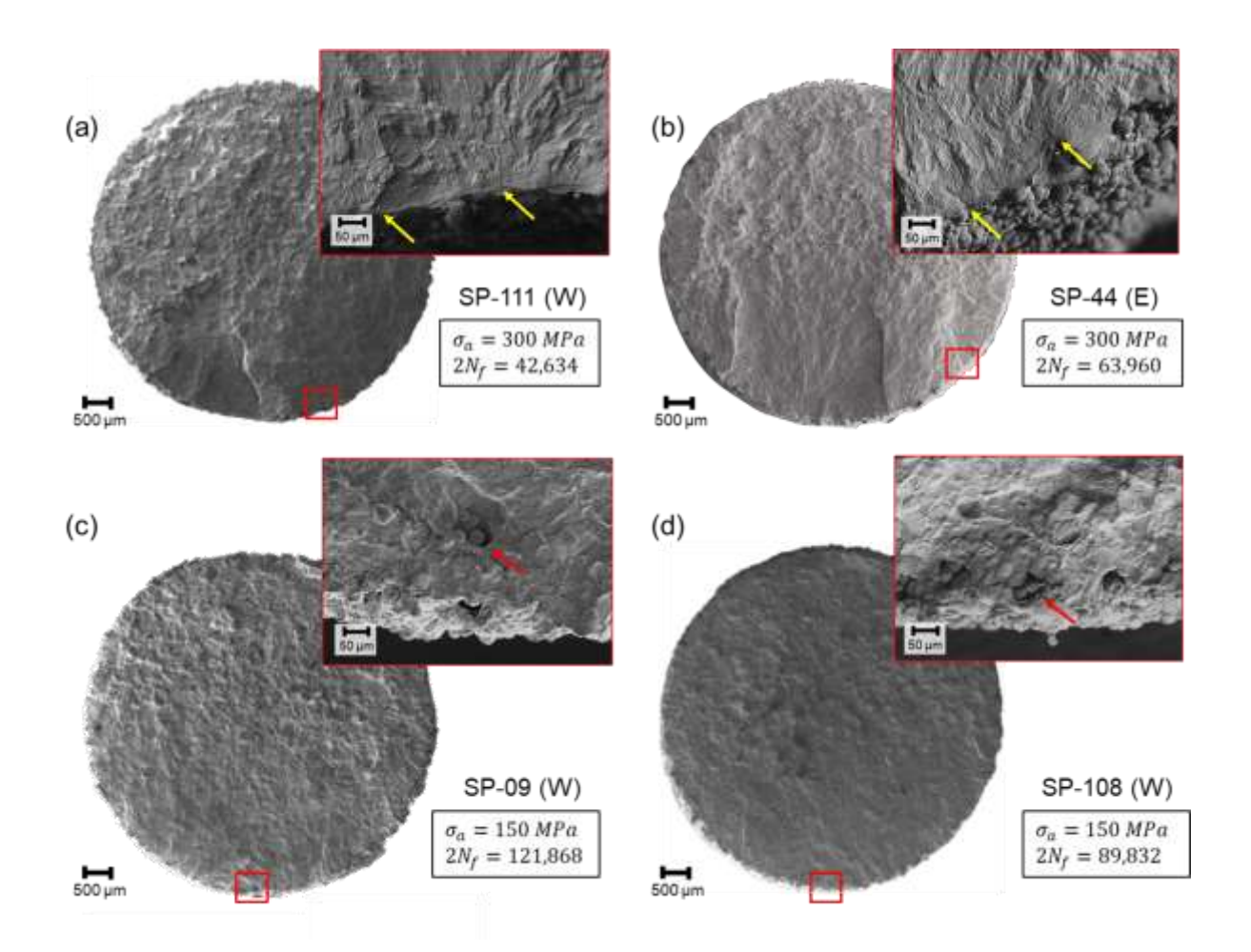


Figure 9: Fatigue fracture surfaces of selected un-machined Ti-5553 west and east specimens. Specimens (a) SP-111 and (b) SP-44 were tested at 300 MPa, while specimens (c) SP-09 and (d) SP-108 were tested at lower stress 150 MPa. Yellow arrows indicate some of the crack initiation sites that are surface anomalies, while red arrows point to volumetric defects on the fracture surface.

## 4.2 Fatigue behavior and the role of volumetric defects

In contrast to the un-machined fatigue specimens, fractographic analysis on machined L-PBF Ti-5553 specimens revealed crack initiation from only volumetric defects. In fact, each fracture surface contained only one crack initiation site. In addition, in most of the machined specimens, the fatigue critical defects were singular, i.e., only one defect existed in each crack initiation site. Figure 10 shows the fracture surfaces of some specimens tested at 600 MPa and 400 MPa. Among all the specimens, the specimen SP-85 (see Figure 10 (b)) appeared to be anomalous, as it contained two defects in the crack initiation site. Given their irregular shapes and close distance, they could have been part of the same lack of fusion defect. Overall, it was observed that the specimens with larger fatigue critical defects tended to have shorter lives. For instance, the specimens SP-116 and SP-85, tested at a stress amplitude of 600 MPa, showed  $\sqrt{\text{area}_{\text{defect,M}}}$  of 62 and 88 µm and fatigue lives of 109,336 and 51,474 reversals, respectively (also shown in Figure 10 (a) and (b)). Nevertheless, some exceptions existed. For example, specimens SP-115 and SP-50, tested at the stress amplitude of 400 MPa, lasted 517,596 and 2,014,460 reversals with the corresponding √area<sub>defect,M</sub> of 61 and 90 μm, respectively. The crack initiation sites could be seen from the fracture surfaces (Figure 10 (c) and (d)), where the critical defect of SP-115 had a large opening to the surface and the critical defect of SP-50 was relatively far from the surface.

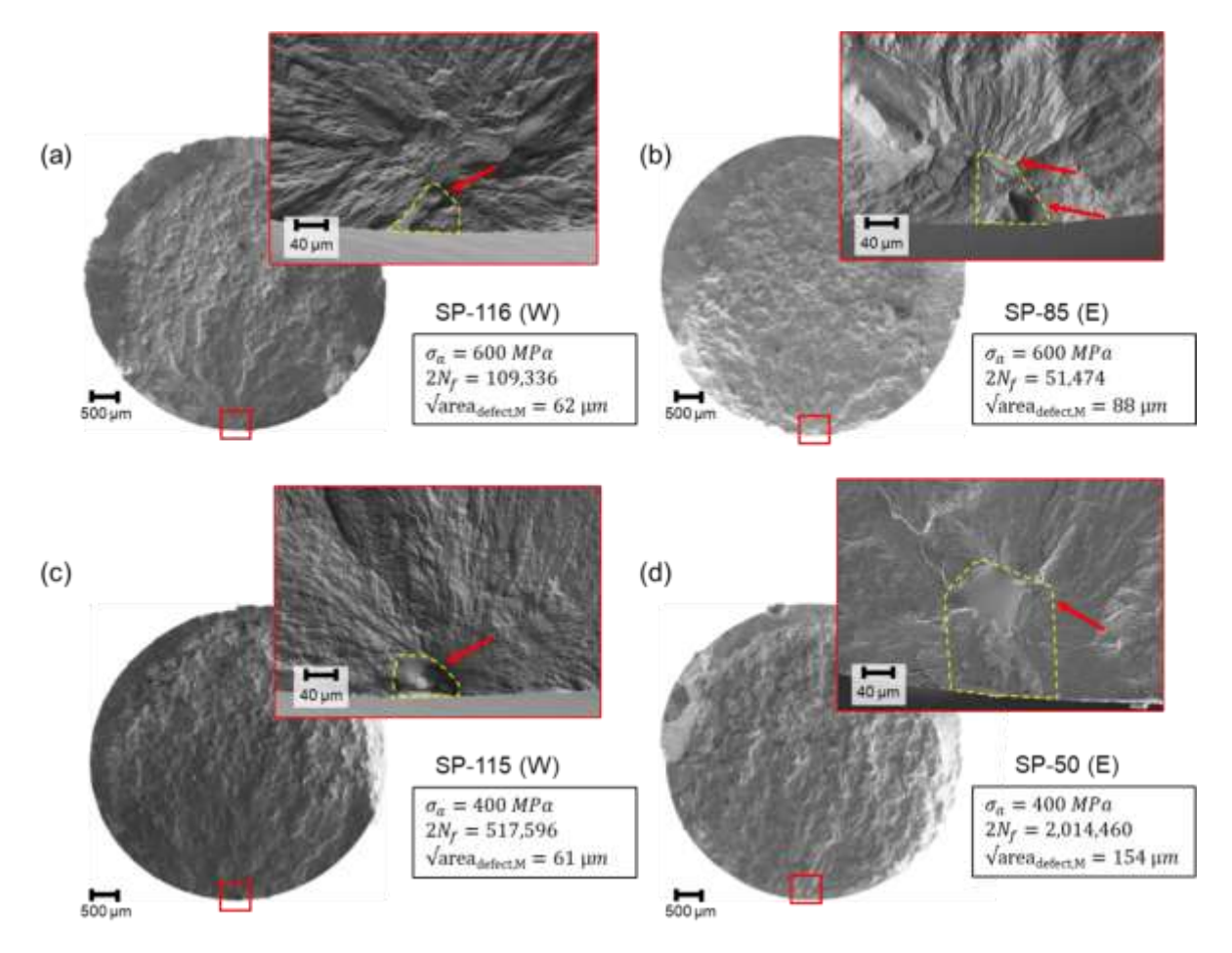


Figure 10: Fatigue fracture surfaces of selected machined L-PBF Ti-5553 west and east specimens. The specimens (a) SP-116 and (b) SP-85 were tested at 600 MPa, while the specimens (c) SP-115 and (d) SP-50 were tested at 400 MPa. Red arrows point to the fatigue critical defects and yellow outline indicates the area<sub>defect,M</sub> following Murakami's approach.

To further investigate the correlation between  $\sqrt{\text{area}_{\text{defect,M}}}$  and the fatigue lives, the stress-life data of machined L-PBF Ti-5553 has been re-plotted in **Figure 11** (a) using the size of the circular markers to indicate  $\sqrt{\text{area}_{\text{defect,M}}}$ . Note that the defects were classified into internal and surface ones according to Murakami et al. [37] (as schematically illustrated in the inset of **Figure 11** (a)), i.e., if the dimension of the defect along the radial direction of the specimen (a) was smaller than its distance from the specimen surface (h) then it was considered as a surface defect; otherwise, it was considered as an internal defect. The internal defects were shown as hollow

markers, and their corresponding h values were labeled. The specimens with internal critical defects had longer fatigue lives than those with surface ones (Figure 11 (a)). Among the specimens with surface critical defects, a trend of larger  $\sqrt{\text{area}_{\text{defect,M}}}$  corresponding to shorter fatigue lives was evident. An exception was the specimen SP-50 (as indicated by the blue arrow in Figure 11 (a) and the fracture surface shown in Figure 10 (d)), whose crack initiating defect behaved like an internal defect. Specifically, the fatigue crack initiation from this defect (a  $\approx 135 \, \mu m$ ) was not accelerated by its proximity to the surface (h  $\approx 120 \, \mu m$ ), and the area<sub>defect</sub> estimated by the contour enveloping the defect's two-dimensional projection (see Figure 10 (d)) could have been an overestimation. The larger defect-shorter fatigue life trend could not be established for the case of internal critical defects due to the lack of adequate data.

The size effect of volumetric defects can be accounted for by some of the existing models [37,53,54]. For instance, the model introduced by Murakami et al. [53] proposes that the effective fatigue limit ( $\sigma_w$ ) is inversely proportional to the ( $\sqrt{\text{area}_{\text{defect},M}}$ )<sup>1/6</sup>, and the relation can be shown as in Eq. 2:

$$\sigma_W = \frac{C_1 (HV + 120)}{\left(\sqrt{area_{defect\,M}}\right)^{1/6}} \tag{2}$$

where HV is the Vickers hardness of the material, and the constant  $C_1$  is  $C_1 = 1.43$  for surface defect and  $C_1 = 1.56$  for internal defect. The stress amplitude has been normalized using  $\sigma_w$ , following the approach by Murakami et al. [53], in an attempt to exclude the size and location effect in the fatigue behavior; and the normalized fatigue behavior is shown in **Figure 11** (b). Although the scatter in fatigue data slightly reduced after the normalization, some scatter still remained, suggesting that defect shape could have also played a role [55].

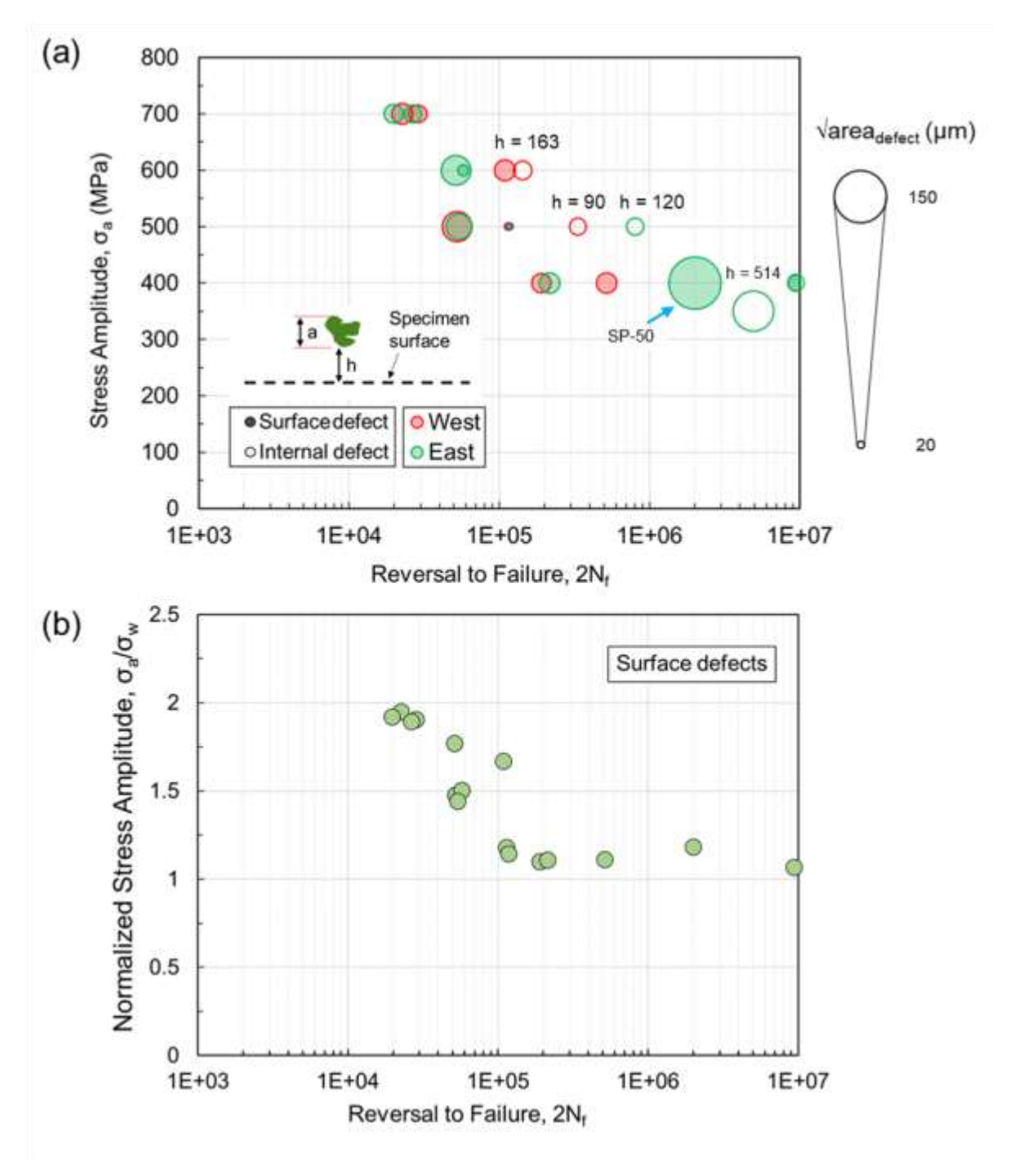


Figure 11: Stress-life fatigue behavior of (a) machined L-PBF Ti-5553 specimens along with  $\sqrt{\text{area}_{\text{defect,M}}}$ ; the value on top of each circle indicates the distance of internal defect relative to the surface in  $\mu$ m, and (b) normalized stress vs. reversal to failure of machined L-PBF Ti-5553.

## 4.3 Extreme value analysis of volumetric defects

Extreme value statistics (EVS) has been used in multiple studies [17,41,56–60] to statistically characterize the size distribution of the most critical defects. The cumulative and probability density functions (F(x) and f(x)) of EVS can be expressed using the Gumbel's distribution, i.e., [61,62]:

$$F(x) = \exp\left(-\exp\left(-\frac{x_i - \lambda}{\delta}\right)\right) \tag{3}$$

$$f(x) = \frac{1}{\delta} \left[ \exp\left(-\frac{x_i - \lambda}{\delta}\right) \times \exp\left(-\exp\left(-\frac{x_i - \lambda}{\delta}\right)\right) \right]$$
 (4)

where  $x_i$  represents the largest defect size measured within a certain volume, the fitting parameters  $\lambda$  and  $\delta$  are the location and scale parameters of the Gumbel distribution, respectively. The present study used the extreme value analysis initially for the fractography data, followed by that for the XCT data. The location and scale parameters indicate the distribution's peak location and variance, respectively. In this study, the parameters,  $\lambda$  and  $\delta$ , were fitted using the method of maximum likelihood [62–64]. This method consists of two steps: (i) calculation of the likelihood length (LL), following Eq. 5, for various combinations of  $\lambda$  and  $\delta$  values corresponding to each defect and (ii) optimization of  $\lambda$  and  $\delta$  values to maximize the LL value. Once the parameters are known, the F(x) and f(x) can be calculated for any defect size using Eq. 3 and 4. Additionally, the probability of a defect exceeding a certain size can be shown in terms of reduced variate ( $Y_i$ ) (Eq. 6).

$$LL = \sum \left( \ln \left( \frac{1}{\delta} \right) - \left( \frac{x_i - \lambda}{\delta} \right) - \exp \left( -\frac{x_i - \lambda}{\delta} \right) \right)$$
 (5)

$$Y_i = -\ln\left(-\ln(\mathsf{F})\right) \tag{6}$$

The probability plots of critical defect size obtained from fractography are presented in **Figure 12** (a) and (b), in terms of reduced variate, Y<sub>i</sub>, and probability density function for west

and east specimens. The reduced variate plots also include a 95% CI, as is indicated by the red and green shaded areas for west and east specimens, respectively in **Figure 12** (a). The location and scale parameters related to **Figure 12** (a) and (b) are provided in **Table 6**. In addition, the  $R^2$  value for the linear fit for west and east specimens were 0.77 and 0.78, respectively. While the  $R^2$  value provides insight into the effectiveness of the fitting parameters ( $\lambda$  and  $\delta$ ) to capture the variability in the critical defect size distribution, it is not sufficient for statistically determining if the critical defect size distribution follows a Gumbel distribution. Therefore, a Lilliefors test was conducted to confirm with a significance level of 0.05. Based on the results, the defect distribution followed a Gumbel distribution for both west and east specimens.

Table 6 also contains the √area<sub>50%</sub>, which represents the defect size corresponding to the 50<sup>th</sup> percentile probability of occurrence, based on extreme value distribution. The √area<sub>50%</sub> is particularly useful for comparing the distribution of defect size across different sample groups, such as specimens fabricated by different processes or subjected to different heat treatments. The √area<sub>50%</sub> values for the Ti-5553 in Figure 12 (a) exceeded those for Ti-64 reported in Ref. [17], suggesting a higher probability of larger critical defects in Ti-5553 than in Ti-64, despite similar fatigue lives (see Figure 8 (c)). Although both west and east specimens exhibited similar location parameters, they had significantly different scale parameters (Table 6), implying a larger variance for the east specimens, as seen in Figure 12 (b).

The differences in the variance may originate from the different criticality between the surface and internal defects, and that their sizes should follow different statistical distributions. For a defect of a given size, it tends to be more detrimental to the fatigue resistance when it is located at or near the specimen surface compared to when it resides deep inside [55,65,66]. In other words, internal critical defects tend to be larger compared to their surface/near-surface counterparts for

the same fatigue life. The probability distribution for the size of the internal critical defects should therefore have a larger mean and a potentially larger variance. The relatively few data points for internal critical defects (4 out of 20 total fatigue fracture surfaces), combined with their relatively large variation in size, could have introduced uncertainties in the statistical quantifications presented in **Figure 12** (a) and (b).

Due to the limited fatigue data for internal critical defects, the statistics of surface critical defects were then separately examined. Figure 12 (c) and (d) show the probability plots of surface critical defect size, with west specimens showing lower  $R^2$  values compared to the east specimens. The higher  $R^2$  values observed in the east specimens likely stemmed from a relatively even distribution of defect sizes, which produced a rather linear relation between the reduced variate and  $\sqrt{a}$  rea. In contrast, the west specimens contained a group of 6 defects with very similar size, which resulted in the data points slightly deviating from the linear relation between reduced variate and  $\sqrt{a}$  rea. However, Lilliefors test indicated that the surface defect size distribution conformed to the Gumbel distribution for both west and east specimens. EVS analysis using only surface critical defect data (Figure 12 (c) and (d)) showed that the defect size distribution did not differ significantly due to part location. Note that this analysis excluded the surface defect of specimen SP-50, which had been identified as an outlier during previous analysis. The similarity in the defect

size distributions aligned well with the fatigue behavior of L-PBF Ti-5553, where no statistically significant difference in fatigue life was observed between west and east specimens.

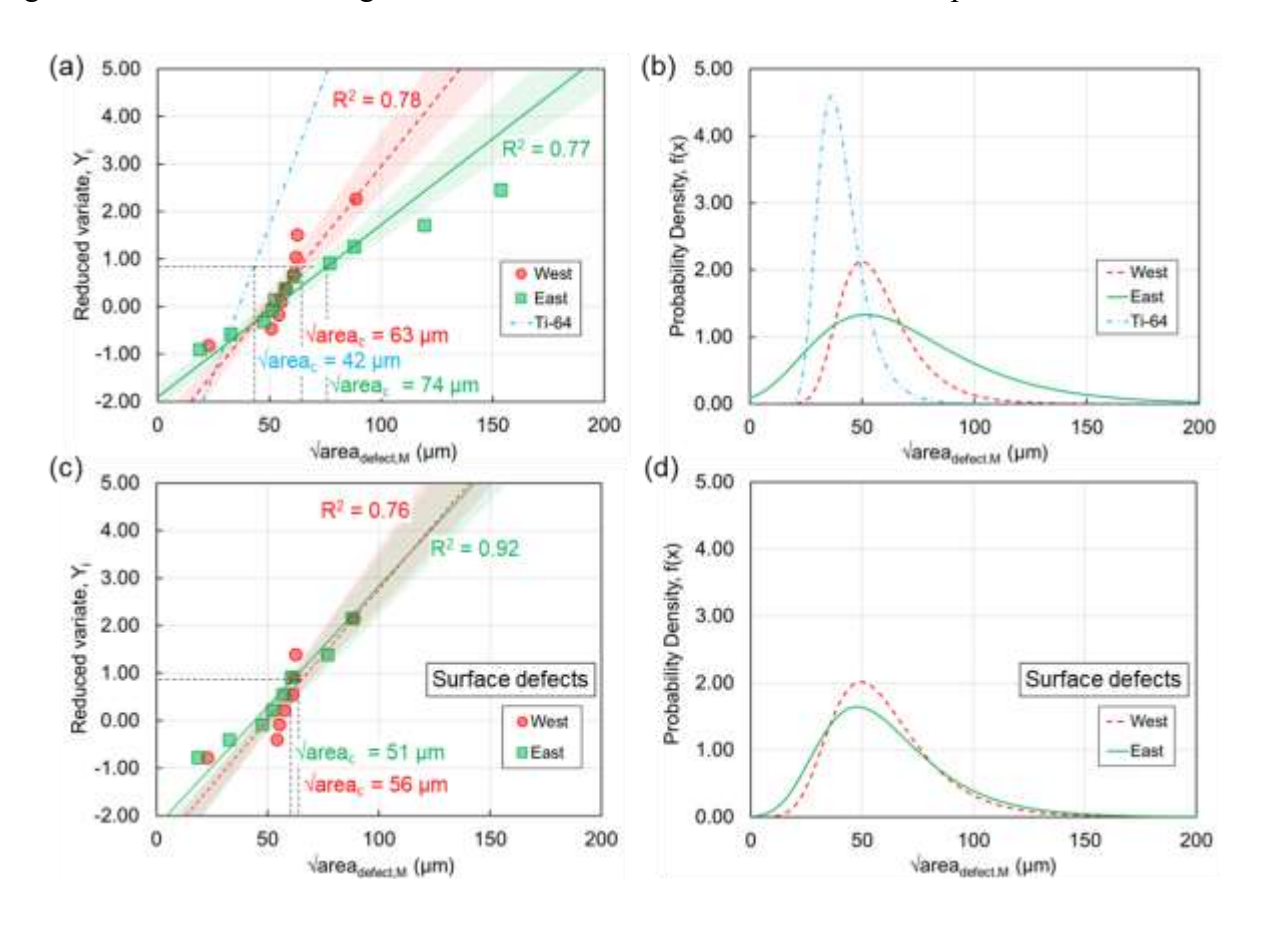


Figure 12: EVS analysis of machined L-PBF Ti-5553 using fractography data: comparison of defect size distribution and probability density function using (a, b) all surface and internal defects, and (c, d) only the surface critical defects for west and east specimens; the comparison has also been made to Ti-64 data presented in Ref. [17].

Although similar defect size distributions were observed between the XCT data of the west and east specimens (**Figure 4** (b)), some location dependencies were still notable among the large outlying defects. These outliers, located at the "tails" of the size distribution curves, often were the fatigue critical ones. The EVS analysis performed on these XCT data was therefore warranted. For this purpose, the block maxima principle was used, following Refs. [56,59]. The overall scanned volumes were subdivided into disk shaped sub volumes of 200 µm thickness perpendicular to the axial direction, resulting in 58 sub volumes in total. Based on the block maxima principle, only

the largest defect from each sub volume was sampled for EVS analysis. The location and scale parameters are listed in **Table 7**. **Figures 13** (a) and (b) show the results of the EVS analysis with relatively high  $R^2$  values for both conditions. Moreover, Lilliefors test indicated a good conformance of the observed defect size distribution to a Gumbel distribution. The  $\sqrt{\text{area}_{50\%}}$  values for west specimens (96  $\mu$ m) was higher than the east ones (52  $\mu$ m), indicating that the probability of having large defects in the west specimens was higher. One should therefore expect, from the statistical analysis performed on the XCT data, an overall lower fatigue resistance for the west specimens, which contradicts with the fatigue data reported in **Figure 11** (a). The discrepancy again should originate from the limited fatigue data where internal defects were critical. The EVS analysis on the surface defects isolated from the XCT data was then performed.

The scanned volumes were divided into internal and surface regions. The surface regions were circular tube with a thickness of 135  $\mu$ m. The value of 135  $\mu$ m was determined based on the maximum distance of surface critical defects observed in the fractography. The probability plots of the extreme defects in the circular tubes for the west and east specimens are presented in **Figure 13** (c) and (d). For both part location, the defect size distribution followed Gumbel's distribution based on Lilliefors tests. Moreover, the defect size distributions of west and east specimens were similar. This was further supported by the  $\sqrt{\text{area}_{50\%}}$  values for west and east specimens, which were found to be 62 and 55  $\mu$ m, respectively. These observations from XCT and fractography suggested that, near the surface, a comparable distribution of extreme defects could be observed, which explained the similar fatigue behavior of L-PBF Ti-5553, irrespective of part location (**Figure 8** (c)).

Table 7: Location ( $\lambda$ ) and scale ( $\delta$ ) parameters of the Gumbel's extreme value distribution for fractography and XCT data.

			λ	δ	√area <sub>50%</sub>
	Surface and internal	East	52.51	27.59	62.65
Eurote amanday	critical defects	West	49.21	17.27	55.54
Fractography —	Surface critical defects	East	44.06	19.77	51.31
		West	49.52	18.22	56.24
XCT	Disk shaped sub volume	East	47.17	14.25	52.39
		West	87.72	24.76	96.79
	Circular tube sub volume	East	53.94	21.77	61.92
		West	46.79	22.75	55.13

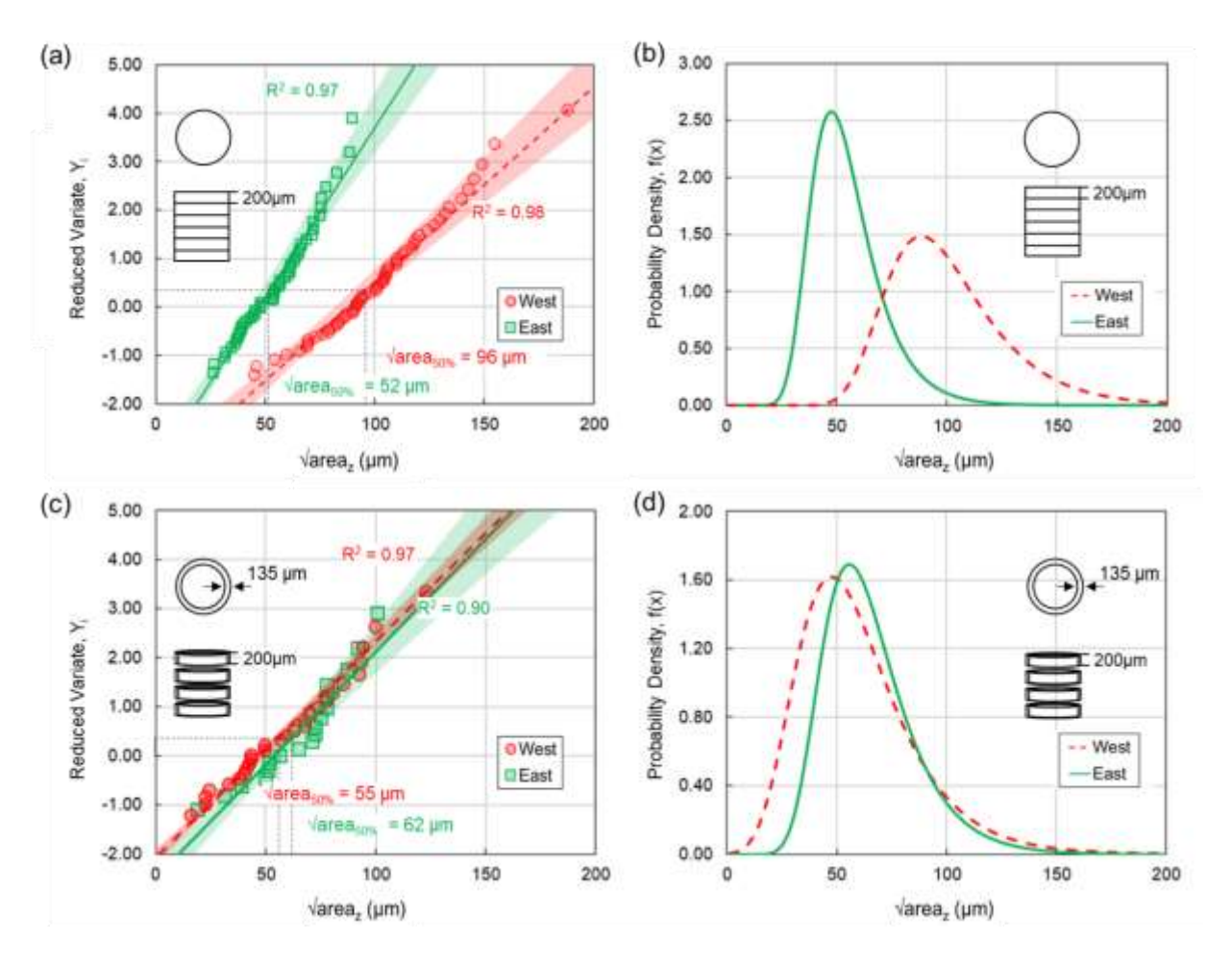


Figure 13: EVS analysis of machined L-PBF Ti-5553 using the XCT data: comparison of defect size distribution and probability density function in sub volumes using (a, b) entire volume, and (c, d) circular tube volume.

#### 5. Conclusion

The present study examined the micro-/defect-structure and mechanical behavior, including tensile and fatigue, of L-PBF Ti-5553. Furthermore, the potential impact of part location was also evaluated. The key findings of this study are as follows:

• The non-heat treated microstructure mostly consisted of columnar  $\beta$  grains. After annealing, the microstructure appeared to be equiaxed with no significant changes in the

phase composition. In addition, no crystallographic textures were found in either non-heat treated or annealed microstructure.

- Ti-5553 showed an acceptable combination of tensile strength (yield and ultimate tensile strengths of ~1125 MPa and ~1220 MPa, respectively) and ductility (elongation to failure of ~14%) compared to its wrought counterparts which either had high strength and low ductility or low strength and high ductility.
- Despite the higher volumetric defect content in west specimens, part location had no significant effect on tensile or fatigue behavior of L-PBF Ti-5553 in either un-machined or machined surface conditions.
- While machining significantly improved the fatigue behavior of L-PBF Ti-5553, the machined specimens exhibited a larger scatter in fatigue life compared to un-machined ones. This difference could be attributed to the overwhelming effect of surface roughness in crack initiation, as well as the lower variability in the un-machined surface texture compared to volumetric defects.
- Extreme value statistical analysis showed that both west and east specimens had statistically similar defect size distributions near the surface which could explain the insensitivity of fatigue life to part location.

#### Acknowledgement

This material is based upon work partially supported by the National Institute of Standards and Technology (NIST) under grant # 70NANB18H220 and the National Science Foundation (NSF) under grant # 2319690.

#### References

- [1] Cotton JD, Briggs RD, Boyer RR, Tamirisakandala S, Russo P, Shchetnikov N, et al. State of the Art in Beta Titanium Alloys for Airframe Applications. Journal of The Minerals, Metals & Materials Society 2015;67:1281–303. https://doi.org/10.1007/s11837-015-1442-4.
- [2] Boyer RR. An overview on the use of titanium in the aerospace industry. Materials Science and Engineering: A 1996;213:103–14.
- [3] Veeck S, Lee D, Boyer R, Briggs R. The castability of Ti-5553 alloy. Advanced Materials and Processes 2004;162:47–9.
- [4] Colombo-Pulgarín JC, Biffi CA, Vedani M, Celentano D, Sánchez-Egea A, Boccardo AD, et al. Beta Titanium Alloys Processed By Laser Powder Bed Fusion: A Review. Journal of Materials Engineering and Performance 2021;30:6365–88. https://doi.org/10.1007/s11665-021-05800-6.
- [5] Shariff T, Cao X, Chromik RR, Wanjara P, Cuddy J, Birur A. Effect of joint gap on the quality of laser beam welded near-β Ti-5553 alloy with the addition of Ti-6Al-4V filler wire. Journal of Materials Science 2012;47:866-75.
- [6] Fatemi A, Molaei R, Sharifimehr S, Shamsaei N, Phan N. Torsional fatigue behavior of wrought and additive manufactured Ti-6Al-4V by powder bed fusion including surface finish effect. International Journal of Fatigue 2017;99:187–201. https://doi.org/10.1016/j.ijfatigue.2017.03.002.
- [7] Li P, Warner DH, Pegues JW, Roach MD, Shamsaei N, Phan N. Towards predicting differences in fatigue performance of laser powder bed fused Ti-6Al-4V coupons from the same build. International Journal of Fatigue 2019;126:284–96. https://doi.org/10.1016/j.ijfatigue.2019.05.004.
- [8] KC S, Nezhadfar PD, Phillips C, Kennedy MS, Shamsaei N, Jackson RL. Tribological behavior of 17–4 PH stainless steel fabricated by traditional manufacturing and laser-based additive manufacturing methods. Wear 2019;440–441:203100. https://doi.org/10.1016/j.wear.2019.203100.
- [9] Qin D, Zhao F, Li Y. The conflicts between strength and ductility of bimodal Ti-5553 alloy with fine equiaxial prior β grains. Materials Science and Engineering: A 2022;841:143074. https://doi.org/10.1016/j.msea.2022.143074.
- [10] Gan Z, Kafka OL, Parab N, Zhao C, Fang L, Heinonen O, et al. Universal scaling laws of keyhole stability and porosity in 3D printing of metals. Nature Communications 2021;12. https://doi.org/10.1038/s41467-021-22704-0.
- [11] Fanning JC. Properties of TIMETAL 555 (Ti-5Al-5Mo-5V-3Cr-0.6 Fe). Journal of Materials Engineering and Performance 2005;14:788–91.
- [12] Buhairi MA, Foudzi FM, Jamhari FI, Sulong AB, Radzuan NAM, Muhamad N, et al. Review on volumetric energy density: influence on morphology and mechanical properties of Ti6Al4V manufactured via laser powder bed fusion. Progress in Additive Manufacturing 2023;8:265–83. https://doi.org/10.1007/s40964-022-00328-0.
- [13] Singla AK, Banerjee M, Sharma A, Singh J, Bansal A, Gupta MK, et al. Selective laser

- melting of Ti6Al4V alloy: Process parameters, defects and post-treatments. Journal of Manufacturing Processes 2021;64:161–87. https://doi.org/10.1016/j.jmapro.2021.01.009.
- [14] Poudel A, Yasin MS, Ye J, Liu J, Vinel A, Shao S, et al. Feature-based volumetric defect classification in metal additive manufacturing. Nature Communications 2022;13:6369. https://doi.org/10.1038/s41467-022-34122-x.
- [15] Soltani-Tehrani A, Shrestha R, Phan N, Seifi M, Shamsaei N. Establishing specimen property to part performance relationships for laser beam powder bed fusion additive manufacturing. International Journal of Fatigue 2021;151:106384. https://doi.org/10.1016/j.ijfatigue.2021.106384.
- [16] Yadollahi A, Shamsaei N. Additive manufacturing of fatigue resistant materials: Challenges and opportunities. International Journal of Fatigue 2017;98:14–31. https://doi.org/10.1016/j.ijfatigue.2017.01.001.
- [17] Soltani-Tehrani A, Habibnejad-Korayem M, Shao S, Haghshenas M, Shamsaei N. Ti-6Al-4V powder characteristics in laser powder bed fusion: The effect on tensile and fatigue behavior. Additive Manufacturing 2022;51:102584. https://doi.org/10.1016/j.addma.2021.102584.
- [18] Zhang B, Meng WJ, Shao S, Phan N, Shamsaei N. Effect of heat treatments on pore morphology and microstructure of laser additive manufactured parts. Material Design & Processing Communications 2019;1:e29. https://doi.org/10.1002/mdp2.29.
- [19] Rao JH, Stanford N. A survey of fatigue properties from wrought and additively manufactured Ti-6Al-4V. Materials Letters 2021;283:128800. https://doi.org/10.1016/j.matlet.2020.128800.
- [20] Sadeghpour S, Abbasi SM, Morakabati M, Bruschi S. Correlation between alpha phase morphology and tensile properties of a new beta titanium alloy. Materials and Design 2017;121:24–35. https://doi.org/10.1016/j.matdes.2017.02.043.
- [21] Lü ZD, Zhang CJ, Du ZX, Han JC, Zhang SZ, Yang F, et al. Relationship between microstructure and tensile properties on a near-β titanium alloy after multidirectional forging and heat treatment. Rare Metals 2019;38:336–42. https://doi.org/10.1007/s12598-018-1159-y.
- [22] Schwab H, Palm F, Kühn U, Eckert J. Microstructure and mechanical properties of the nearbeta titanium alloy Ti-5553 processed by selective laser melting. Materials & Design 2016;105:75–80. https://doi.org/10.1016/j.matdes.2016.04.103.
- [23] Alcântara EGA. Characterization of the fatigue behavior of additively manufactured β-metastable titanium alloy Ti-5Al-5V-5Mo-3Cr on different length scales. Technical University of Berlin, 2024.
- [24] Hasanabadi M. Process Optimization, Numerical Modelling, and Microstructure Control in Laser Powder Bed Fusion of Ti-5553 Parts. University of Waterloo, 2024.
- [25] Carlton HD, Klein KD, Elmer JW. Evolution of microstructure and mechanical properties of selective laser melted Ti-5Al-5V-5Mo-3Cr after heat treatments. Science and Technology of Welding and Joining 2019;24:465–73.

- https://doi.org/10.1080/13621718.2019.1594589.
- [26] Ramachandiran N, Asgari H, Dibia F, Eybel R, Muhammad W, Gerlich A, et al. Effects of post heat treatment on microstructure and mechanical properties of Ti5553 parts made by laser powder bed fusion. Journal of Alloys and Compounds 2023;938:168616. https://doi.org/10.1016/j.jallcom.2022.168616.
- [27] Veiga C, Davim JP, Loureiro AJR. Properties and applications of titanium alloys: a brief review. Rev Adv Mater Sci 2012;32:133–48.
- [28] Clément N. Phase transformations and mechanical properties of the Ti-5553 β-metastable titanium alloy 2010:314 p.
- [29] Huang C, Zhao Y, Xin S, Tan C, Zhou W, Li Q, et al. Effect of microstructure on high cycle fatigue behavior of Ti–5Al–5Mo–5V–3Cr–1Zr titanium alloy. International Journal of Fatigue 2017;94:30–40. https://doi.org/10.1016/j.ijfatigue.2016.09.005.
- [30] ASTM International. ASTM B822-20, Standard test method for particle size distribution of metal powders and related compounds by light scattering. West Conshohocken, PA: 2020.
- [31] ASTM International. ASTM D7891 Standard test method for shear testing of powders using the Freeman Technology FT4 powder rheometer shear cell. West Conshohocken, PA: 2015.
- [32] Freeman Technology. FT4 Powder Rheometer Summary of Methodologies 2008 n.d.
- [33] Jones NG, Dashwood RJ, Dye D, Jackson M. Thermomechanical processing of Ti-5Al-5Mo-5V-3Cr. Materials Science and Engineering A 2008. https://doi.org/10.1016/j.msea.2008.01.055.
- [34] ASTM International. ASTM E8 / E8M-21, Standard Test Methods for Tension Testing of Metallic Materials. West Conshohocken, PA: 2021.
- [35] ASTM International. ASTM E466-15, Standard practice for conducting force controlled constant amplitude axial fatigue tests of metallic materials. West Conshohocken, PA: 2015.
- [36] ASTM. ASTM E739-10 Standard Practice for Statistical Analysis of Linear Or Linearized Stress-Life (SN) and Strain-Life ([epsilon]-N) Fatigue Data. vol. 10. 2010.
- [37] Murakami Y. Metal Fatigue. Elsevier; 2002. https://doi.org/10.1016/B978-0-08-044064-4.X5000-2.
- [38] Brika SE, Letenneur M, Dion CA, Brailovski V. Influence of particle morphology and size distribution on the powder flowability and laser powder bed fusion manufacturability of Ti-6Al-4V alloy. Additive Manufacturing 2020;31:100929. https://doi.org/10.1016/j.addma.2019.100929.
- [39] Soltani-Tehrani A, Pegues J, Shamsaei N. Fatigue behavior of additively manufactured 17-4 PH stainless steel: The effects of part location and powder re-use. Additive Manufacturing 2020;36:101398. https://doi.org/10.1016/j.addma.2020.101398.
- [40] Murakami Y. Material defects as the basis of fatigue design. International Journal of Fatigue 2012;41:2–10. https://doi.org/10.1016/j.ijfatigue.2011.12.001.

- [41] Sanaei N, Fatemi A. Analysis of the effect of internal defects on fatigue performance of additive manufactured metals. Materials Science and Engineering: A 2020;785:139385. https://doi.org/10.1016/j.msea.2020.139385.
- [42] Li P, Lee PD, Maijer DM, Lindley TC. Quantification of the interaction within defect populations on fatigue behavior in an aluminum alloy. Acta Materialia 2009;57:3539–48. https://doi.org/10.1016/j.actamat.2009.04.008.
- [43] Chu F, Zhang K, Shen H, Liu M, Huang W, Zhang X, et al. Influence of satellite and agglomeration of powder on the processability of AlSi10Mg powder in Laser Powder Bed Fusion. Journal of Materials Research and Technology 2021;11:2059–73. https://doi.org/10.1016/j.jmrt.2021.02.015.
- [44] Sen M, Suman S, Banerjee T, Bhattacharjee A, Kar SK. Tensile deformation mechanism and failure mode of different microstructures in Ti-5Al-5Mo-5V-3Cr alloy. Materials Science and Engineering A 2019;753:156-67. https://doi.org/10.1016/j.msea.2019.03.003.
- [45] Carrion PE, Shamsaei N, Daniewicz SR, Moser RD. Fatigue behavior of Ti-6Al-4V ELI including mean stress effects. International Journal of Fatigue 2017;99:87–100. https://doi.org/10.1016/j.ijfatigue.2017.02.013.
- [46] Foltz JW, Welk B, Collins PC, Fraser HL, Williams JC. Formation of grain boundary α in β Ti alloys: Its role in deformation and fracture behavior of these alloys. Metallurgical and Materials Transactions A 2011;42:645–50. https://doi.org/10.1007/s11661-010-0322-3.
- [47] Chen Y, Du Z, Xiao S, Xu L, Tian J. Effect of aging heat treatment on microstructure and tensile properties of a new β high strength titanium alloy. Journal of Alloys and Compounds 2014;586:588–92. https://doi.org/10.1016/j.jallcom.2013.10.096.
- [48] Ramachandiran N, Asgari H, Dibia F, Eybel R, Ma H, Gerlich A, et al. Influence of α case and transition zone microstructures on tensile properties in laser powder bed fused and heat-treated Ti-5553 parts. Materials Characterization 2023;199:112834. https://doi.org/10.1016/j.matchar.2023.112834.
- [49] Stephens RI, Fatemi A, Stephens RR, Fuchs HO. Metal fatigue in engineering. John Wiley & Sons; 2000.
- [50] Molaei R, Fatemi A, Sanaei N, Pegues J, Shamsaei N, Shao S, et al. Fatigue of additive manufactured Ti-6Al-4V, Part II: The relationship between microstructure, material cyclic properties, and component performance. International Journal of Fatigue 2020;132:105363. https://doi.org/10.1016/j.ijfatigue.2019.105363.
- [51] Lee S, Rasoolian B, Silva DF, Pegues JW, Shamsaei N. Surface roughness parameter and modeling for fatigue behavior of additive manufactured parts: A non-destructive datadriven approach. Additive Manufacturing 2021;46:102094. https://doi.org/10.1016/j.addma.2021.102094.
- [52] Kahlin M, Ansell H, Basu D, Kerwin A, Newton L, Smith B, et al. Improved fatigue strength of additively manufactured Ti6Al4V by surface post processing. International Journal of Fatigue 2020;134:105497. https://doi.org/10.1016/j.ijfatigue.2020.105497.
- [53] Murakami Y, Takagi T, Wada K, Matsunaga H. Essential structure of S-N curve: Prediction

- of fatigue life and fatigue limit of defective materials and nature of scatter. International Journal of Fatigue 2021;146:106138. https://doi.org/10.1016/j.ijfatigue.2020.106138.
- [54] El Haddad MH, Topper TH, Smith KN. Prediction of non propagating cracks. Engineering Fracture Mechanics 1979;11:573–84. https://doi.org/10.1016/0013-7944(79)90081-X.
- [55] Shao S, Poudel A, Shamsaei N. A linear elastic finite element approach to fatigue life estimation for defect laden materials. Engineering Fracture Mechanics 2023;285:109298. https://doi.org/10.1016/j.engfracmech.2023.109298.
- [56] Romano S, Brandão A, Gumpinger J, Gschweitl M, Beretta S. Qualification of AM parts: Extreme value statistics applied to tomographic measurements. Materials & Design 2017;131:32–48. https://doi.org/10.1016/j.matdes.2017.05.091.
- [57] Romano S, Brückner-Foit A, Brandão A, Gumpinger J, Ghidini T, Beretta S. Fatigue properties of AlSi10Mg obtained by additive manufacturing: Defect-based modelling and prediction of fatigue strength. Engineering Fracture Mechanics 2018;187:165–89. https://doi.org/10.1016/j.engfracmech.2017.11.002.
- [58] Pegues JW, Shao S, Shamsaei N, Sanaei N, Fatemi A, Warner DH, et al. Fatigue of additive manufactured Ti-6Al-4V, Part I: The effects of powder feedstock, manufacturing, and post-process conditions on the resulting microstructure and defects. International Journal of Fatigue 2020;132:105358. https://doi.org/10.1016/j.ijfatigue.2019.105358.
- [59] Minerva G, Awd M, Tenkamp J, Walther F, Beretta S. Machine learning-assisted extreme value statistics of anomalies in AlSi10Mg manufactured by L-PBF for robust fatigue strength predictions. Materials & Design 2023;235:112392. https://doi.org/10.1016/j.matdes.2023.112392.
- [60] Soltani-Tehrani A, Isaac JP, Tippur HV, Silva DF, Shao S, Shamsaei N. Ti-6Al-4V powder reuse in laser powder bed fusion (L-PBF): The effect on porosity, microstructure, and mechanical behavior. International Journal of Fatigue 2023;167:107343. https://doi.org/10.1016/j.ijfatigue.2022.107343.
- [61] Gumbel EJ. Statistics of Extremes. Columbia university press; 1958.
- [62] Rao SS. Reliability engineering. vol. 152. Pearson London; 2015.
- [63] Lindgren BW. Statistical theory. 2nd ed. New York: 1976.
- [64] Cheng R. Non-standard parametric statistical inference. Oxford University Press; 2017.
- [65] Sanaei N, Fatemi A. Defects in additive manufactured metals and their effect on fatigue performance: A state-of-the-art review. Progress in Materials Science 2021;117:100724. https://doi.org/10.1016/j.pmatsci.2020.100724.
- [66] Tammas-Williams S, Withers PJ, Todd I, Prangnell PB. The influence of porosity on fatigue crack initiation in additively manufactured titanium components. Scientific Reports 2017;7:7308. https://doi.org/10.1038/s41598-017-06504-5.